

Supplementary information

Bubble Nucleation and Growth in Nanochannels

Bo Bao^{1,†}, Seyed Hadi Zandavi^{1,†}, Huawei Li¹, Junjie Zhong¹, Arnav Jatukaran¹, Farshid Mostowfi², David Sinton^{1,*}

¹Department of Mechanical and Industrial Engineering, University of Toronto, M5S3G8 Canada

²Schlumberger-Doll Research, Cambridge, Massachusetts, 02139 USA

* corresponding author: sinton@mie.utoronto.ca

† Bo Bao and Seyed Hadi Zandavi contributed equally to this work.

Section S1: Nomenclature

Section S2: Nanofluidic Chip Fabrication Procedure

Section S3: Characterization of Nanochannels

Section S4: Temperature Measurement

Section S5: Experimental Procedure

Section S6: Intensity difference between liquid and vapor phase

Section S7: Fluid dynamic model of vapor bubble column growth

Section S8: Supplemental data

S1 - Nomenclature

Table S1. Nomenclature

Symbol	Meaning	Symbol	Meaning
A	cross sectional area of the channel	P_{res}	pressure in the reservoir
A_{cond}	area of heat conduction	P_{sat}	saturation pressure
$C.P.$	critical point	$P_{\text{v}}(t)$	pressure in vapor phase vs. time
d_g	thickness of glass	R	universal gas constant
d_{si}	thickness of silicon	R_c	critical radius
D_l	distance from liquid-vapor interface to reservoir	T	temperature
dN_{v}/dt	evaporation rate at the liquid-vapor interface	T_{sat}	saturation temperature
$(dP/dV)_T$	slope of P-V diagram at a constant temperature	T_{high}	temperature of copper heater
f	flow friction	T_{low}	temperature of copper chiller
h	channel depth	T_l	temperature of liquid phase
k_B	Boltzmann constant	t_N	waiting time for bubble nucleation
K_{cp}	thermal conductivity of copper	$u_{\text{liq}}(t)$	bulk liquid velocity vs. time
K_g	thermal conductivity of glass	V	volume
K_{si}	thermal conductivity of silicon	V_l	volume of liquid under observation
l_B	vapor bubble column length	W	channel width
l_L	position of left liquid-vapor interface	Z	constant rate
l_R	position of right liquid-vapor interface	Γ	liquid-vapor surface tension
M	molar mass of propane	ΔP_{cav}	cavitation pressure
N_{v}	moles of vapor	ΔT_{sup}	superheat temperature
P	Pressure	μ	viscosity of liquid
P_l	pressure of liquid phase	ρ_l	density of liquid phase
P_N^L	nucleation pressure predicted by nucleation theory	σ_T	temperature deviation

S2 - Nanofluidic chip fabrication procedure

Fig. S1 shows the schematics of fabrication process. The nanochannels and microchannels are fabricated in 4-inch-diameter and 1-mm-thick silicon wafers with two-step deep reactive ion etching (DRIE). The positive photoresist S1818 is used for both etching steps. Specifically, 1), nanochannel patterns are etched into silicon wafers by (a) photolithography and (b) DRIE. The depths of nanochannels (~ 88 nm) can be accurately controlled by the etching power and time; 2), the service microchannels patterns are etched into the nanochannel-patterned silicon wafers by (c) photolithography and (d) DRIE; 3), inlet and outlet holes are drilled through the silicon substrate (e); 4), the silicon substrate and a piece of borofloat cover glass are cleaned in Piranha solution ($\text{H}_2\text{SO}_4:\text{H}_2\text{O}_2 = 3:1$) for 1 hour (f); finally, the silicon substrate is bonded to the cover glass via anodic bonding process (g) at pressure of 10^{-7} bar for about 20 minutes at 400°C , with a voltage of 600 V and a current of 4 mA.

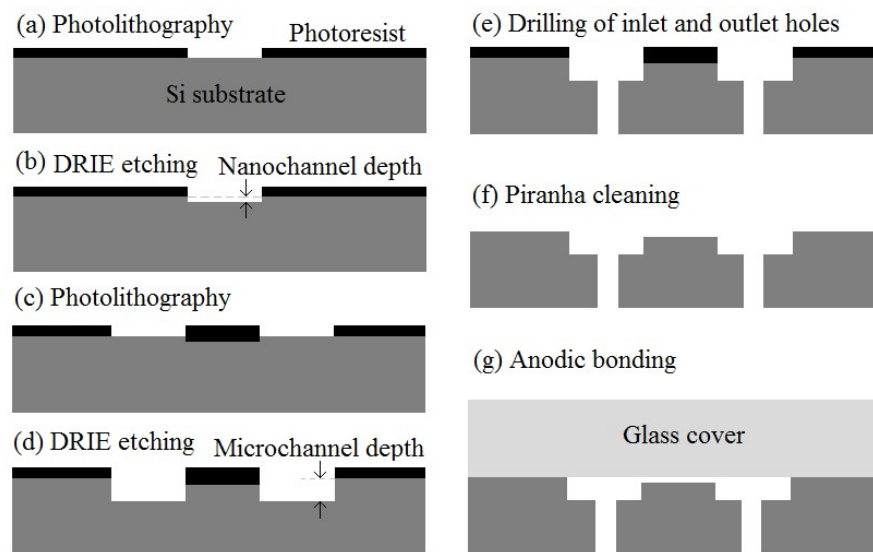


FIG. S1 Schematics of nanochip fabrication process.

S3 - Characterization of nanochannels

The presence of surface corrugations can cause heterogeneous nucleation. Therefore, it is important to characterize surface roughness of nanochannels. In this study, nanochannel surfaces are characterized by Atomic Force Microscopy (AFM) (Hitachi 5100N). AFM measurements are performed over a scanning area of $50 \times 50 \mu\text{m}^2$ on the etched silicon wafer after step (f) shown in Fig. S1. Depth and roughness are measured across multiple nanochannels at randomly chosen intervals. Data are processed and analyzed using AFM analysis software (Gwyddion).

Fig. S2 a) shows the nanochannel profile image and extracted profiles at three locations. The average channel depth is 88 nm with a relative standard deviation of 3%, which indicates the depths are consistent across all the measurement points. Fig. S2 b) shows the AFM image of nanochannel bottom surface and extracted profiles at three locations. The average roughness and the root mean square (RMS) roughness are 0.77 nm and 1.05 nm, respectively. In order to investigate the effect of nanochannel height in roughness, the roughness measurements are performed in nanochannels with different depths of 72, 88 and 118 nm. In all the cases, the surface roughness is 1 nm RMS, indicating that the roughness is a very small fraction of the fabricated channel height in this range.

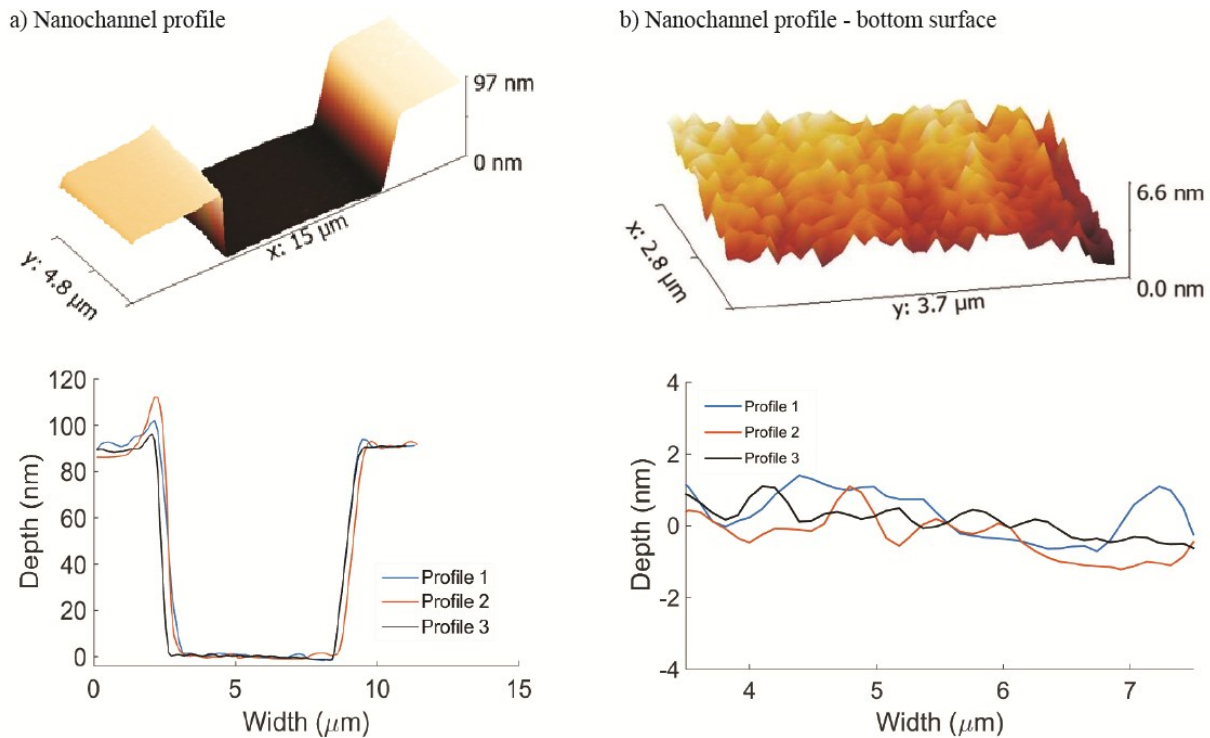


FIG. S2 Characterization of nanochannels by AFM.

The nanochannel is also characterized by Scanning Electron Microscopy (SEM). Fig. S3 shows the cross-sectional view of nanochannel between glass and silicon. The cross-section of the channel indicates a high aspect ratio (width/depth $\cong 80$). The zoomed-in image indicates the nanochannel has a clean and smooth surface.

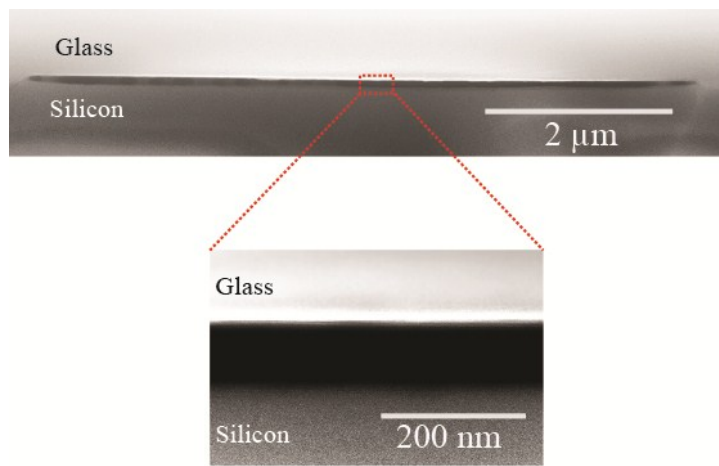


FIG. S3 Characterization of nanochannels by SEM.

S4 - Temperature measurement

Temperatures are systematically measured by thermocouples at four positions around the observation window, $T_{\text{high-a}}$, $T_{\text{high-b}}$, $T_{\text{high-c}}$ and T_d . Schematics of temperature measurements is illustrated in Fig. S4.

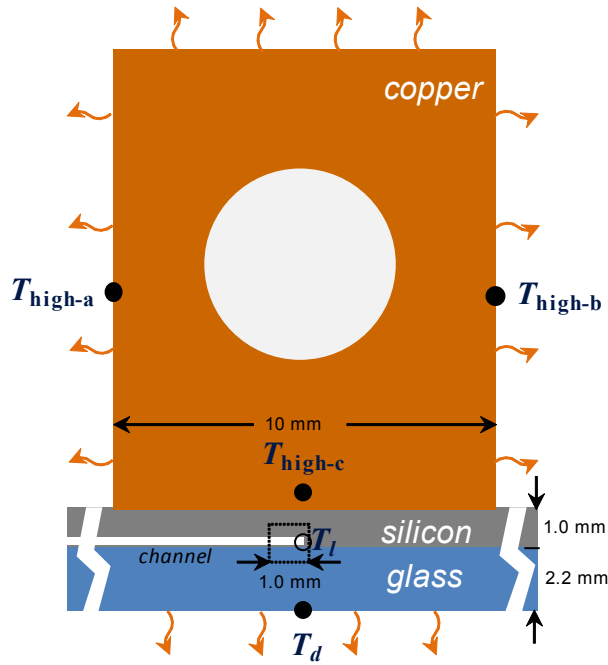


FIG. S4. Temperature measurements at four positions, $T_{\text{high-a}}$, $T_{\text{high-b}}$, $T_{\text{high-c}}$ and T_d (labelled as solid circles). The dotted line window indicates the 1-mm-long field of view under microscope.

First, $T_{\text{high-a}}$ and $T_{\text{high-b}}$ are two measurement points attached on the center of two side walls of the copper heater. Second, $T_{\text{high-c}}$ is the measurement point inside a hole drilled inside the copper heater. Specifically, the measurement hole (diameter is same as the thermocouple, length is half of copper heater width) is drilled inside the copper heater just 0.5 mm above the bottom surface of the copper heater. A K-type thermocouple is inserted inside the measurement hole with thermo-conductive paste. Lastly, T_d is the measurement point attached on the bottom surface of the glass at the location just beneath the field of view. All the temperatures are measured using K-type thermocouples and logged for a 15-minute period. The recorded data is used to calculate average values and standard deviations. The results are shown in Table S2.

Table S2. Measured temperatures

$T_{\text{high-a}} = T_{\text{high-b}}$ (K)	σ_{T_d} (K)	$T_{\text{high-c}}$ (K)	σ_{T_c} (K)	T_d (K)	σ_{T_d} (K)	$T_{\text{high-a}} - T_{\text{high-c}}$ (K)	$T_{\text{high-c}} - T_d$ (K)
343.0	0.076	342.4	0.047	338.6	0.097	0.6	3.8
347.0	0.044	346.3	0.050	342.1	0.104	0.7	4.2
352.0	0.046	351.3	0.060	346.7	0.091	0.7	4.6
357.0	0.062	356.2	0.050	351.2	0.102	0.8	5.0
362.0	0.052	361.2	0.046	355.8	0.085	0.8	5.4
367.0	0.089	366.1	0.058	360.3	0.057	0.9	5.8
372.0	0.101	371.0	0.100	365.3	0.116	1.0	5.7
377.0	0.132	375.9	0.080	369.9	0.128	1.1	6.0

The temperature of liquid T_l in the nanochannel can be determined by the measured temperatures (T_{high-c} and T_d) and 1-dimensional (1D) heat conduction model with known properties (See Table S3) as described below:

Table S3. Properties used in 1D heat conduction model

thickness of glass, d_g (mm)	2.2
thickness of silicon, d_{si} (mm)	1.0
thermal conductivity of glass, K_g (W/m/K)	0.94
thermal conductivity of silicon, K_{si} (W/m/K)	148

The heat flow rate \dot{Q} through the silicon and glass layers

$$\dot{Q} = \frac{T_{high-c} - T_d}{R_g + R_{si}} = \frac{T_{high-c} - T_l}{R_{si}}$$

where,

$$R_g = \frac{d_g}{K_g * A_{cond}}$$

$$R_{si} = \frac{d_{si}}{K_{si} * A_{cond}}$$

The temperature of liquid T_l in the nanochannel can be calculated as

$$\begin{aligned} T_l &= T_{high-c} - (T_{high-c} - T_d) \frac{R_{si}}{R_{si} + R_g} \\ &= T_{high-c} - (T_{high-c} - T_d) \frac{\frac{d_{si}}{K_{si}}}{\frac{d_{si}}{K_{si}} + \frac{d_g}{K_g}} \\ &= T_{high-c} - (T_{high-c} - T_d) \times 2.9 \times 10^{-3} \end{aligned}$$

By using the maximum difference of $(T_{high-c} - T_d) = 6.0$ °C, as shown in Table S2, the term of $(T_{high-c} - T_d) \times 2.9 \times 10^{-3}$ is 0.017 °C, which is negligible. Therefore, the temperature of liquid in the nanochannel is the same as that measured at the base of the copper heater (within experimental error):

$$T_l = T_{high-c}$$

It is noteworthy that the ratio of thermal conductivity of silicon K_{si} to that of glass K_g is 157. Therefore, the temperature of liquid T_l in the nanochannel on the silicon wafer is very close to the heater bottom surface temperature and significantly different from the temperature of bottom of glass T_d .

S5 - Experimental procedure

The assembled nanofluidic chip is installed on a customized manifold enabling appropriate sealing for high pressures. The chip and manifold are connected to a sample source cylinder (research grade propane, Praxair 99.99%), syringe pump (TELEDYNE ISCO MODEL 260D), and isolation piston cylinder (HIP 70C3-10-P) via tubing and valves. The tubing, pump, piston chambers and valves are cleaned thoroughly before connecting to the nanofluidic chip. The entire system is vacuumed at 1.6×10^{-3} MPa (PFPE RV8) for 3 hours before each set of experiments to minimize the residual air in the system. Research-grade liquid propane is filled into the nanochannels. In the initial filling to a brand new chip, the temperature and pressure are set far below the liquid-vapor saturation line to ensure that vapor propane diffused and completely filled the nanochannel. The pressure is maintained and controlled by the ISCO syringe pump and monitored by a high speed pressure transducer (Omega PX409). The isolation piston cylinder is used between the pump and chip to avoid contamination of the sample. The temperature in the chip is controlled by a pair of copper-made heater and chiller clamped on the top of the chip.

A high-speed camera (PCO 1200S, 50 frames per second) connected to the optical microscope (LEICA DMI 6000B) with a $10 \times$ objective lens is used to observe the bubble nucleation and to record the vapor column growth. The field of view ($\sim 1.0 \times 1.0$ mm) is located on the dead-end portion of the group of 10 nanochannels. To ensure bubble nucleation initiated within the field of view, we introduced a temperature difference across the chip by pairing a heater and a chiller. The entrance region of the nanochannels is set at a lower temperature (T_{low}) using the chiller with a water circulating bath. The dead-end portion of the nanochannel is set at a high temperature (T_{high}). The temperature T_{high} is controlled by the heater with a water / silicon oil circulator bath. The dead-end of nanochannel is located at center of the 10-mm long heater. In other words, the heater covers the last 5 mm length of the nanochannels. Both the heater and the chiller are tightly contacted with the silicon side of the chip using mechanical clamp to minimize contact thermal resistance.

The temperature of the chiller water bath is set constant at 288 K. The temperature of copper heater T_{high} is set at different temperatures ranging from 342.4 to 375.9 K. For each temperature, T_{high} , the pressure is initially set at a point above the saturation pressure of T_{high} to ensure that the fluid in all the nano- and micro-channels is in the liquid phase. For each temperature, T_{high} is kept constant for 1 hour to reach thermal equilibrium before conducting experiments. The pressure is gradually decreased in steps of 0.1 MPa. At each pressure step, 15-minute waiting time is given to observe bubble nucleation. Cycles of pressure drawdown are repeated until bubble nucleation occurs. Fig. S5 shows an example of one round of operation pressures in the propane phase diagram; hollow symbols indicate that bubble nucleation is not detected within 15 minutes of observation while the solid symbols indicate that vapor bubble nucleated within 15 minutes. In total, eight different temperatures ($T_i = 342.4, 346.3, 351.3, 356.2, 361.2, 366.1, 371.0$ and 375.9 K) are performed. Table S4 summarizes the complete bubble nucleation conditions. Note that the horizontal axis in Fig. S5 is the temperature of liquid inside dead-end portion of nanochannels (T_l), which equals to the temperature of base of copper heater ($T_{\text{high-c}}$). The details of temperature measurement are presented in the section of "Temperature measurement".

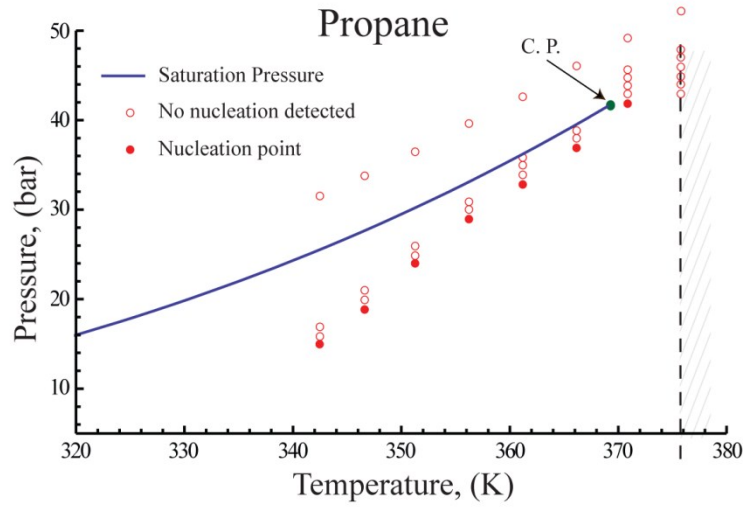


FIG. S5 Operation pressures of pressure-drawdown experiment

Table S4. Bubble nucleation conditions

T_l (K)	P_l (MPa)	ΔT_{sup} (K)	ΔP_{cav} (MPa)
342.4	1.30	31.6	1.26
346.3	1.75	22.3	1.01
351.3	2.20	16.4	0.83
356.2	2.65	12.0	0.68
361.2	3.10	8.8	0.54
366.1	3.70	4.1	0.28
371.0	4.20	1.9	0.05
375.9	-	-	-

S6 - Intensity difference between liquid and vapor phase

The relative intensity difference between liquid and vapor is plotted versus temperature, as shown in Fig. S6. All the intensity of vapor side is normalized to one in order to have a common base for comparison. It can be seen that the relative intensity of liquid side increases as temperature climbs up towards to the critical point. This is because the liquid-vapor interfacial tension decreases and the interface becomes visually less sharp when the temperature approaches to critical point where liquid and vapor become a homogeneous supercritical phase. The two insets show the relative intensity difference between two phases at the lowest and highest temperature conditions, i.e. 342.4 and 371.0 K.

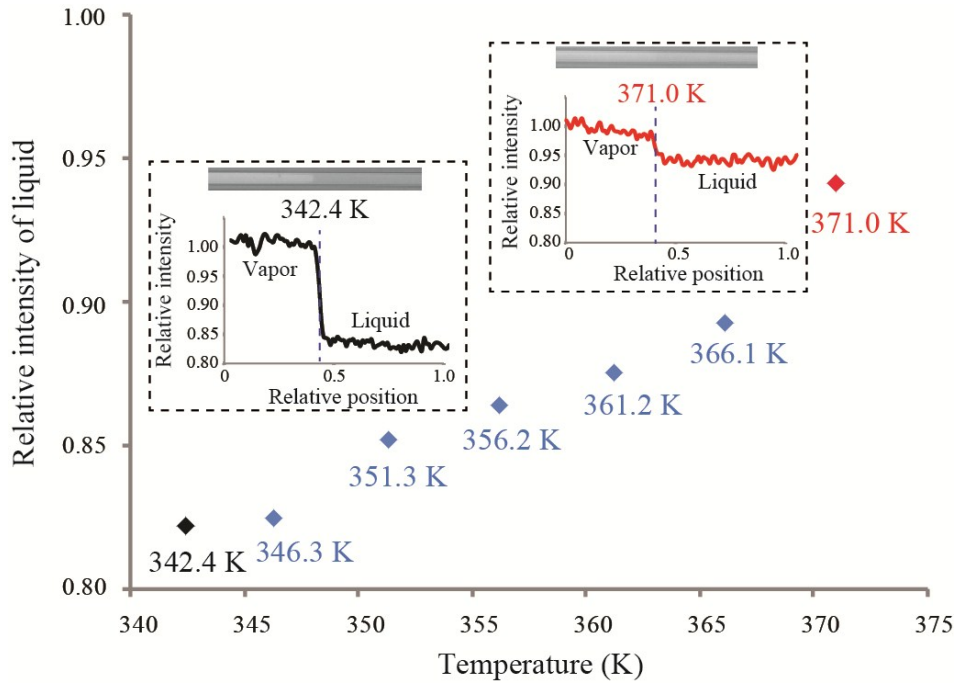


FIG. S6. Intensity profile across liquid-vapor interface

S7 - Fluid dynamic model of vapor bubble column growth

Fig. 4a shows Type A growth of the vapor bubble column at five different temperatures. Early in the transient start-up regime, the pressure in the bubble is near its maximum, and the rate of bubble expansion is governed by the balance of pressure force and surrounding fluid inertia [1]. The bulk liquid flow in the nanochannel is approximated as one-dimensional flow, as illustrated in the inset of Fig. 4b. The liquid phase pressure at the entrance of the nanochannel is same as the pressure in the reservoir P_{res} , and the pressure in the vapor phase $P_v(t)$ is assumed to be uniform across the bubble. The resulting governing equation of the liquid motion in the nanochannel is [2]

$$D_l \rho_l \frac{du_{liq}(t)}{dt} + f u_{liq}(t) = P_v(t) - P_{res}, \quad (4)$$

where $u_{liq}(t)$ is the bulk liquid velocity, $D_l = 35$ mm is the distance from the liquid-vapor interface to the reservoir and can be assumed to be constant since $D_l \gg l_B$, and $f = 12\mu D_l/h^2$ is the flow friction in rectangular channels, where μ is the bulk viscosity [3].

The time derivative of the bubble length can be viewed as a summation of $u_{liq}(t)$ and a component related to the evaporation at the liquid-vapor interface

$$\frac{dl_B(t)}{dt} = u_{liq}(t) + \frac{M}{A\rho_l} \frac{dN_v(t)}{dt}, \quad (5)$$

where N_v is the moles of vapor and dN_v/dt is the evaporation rate, M is the molar mass of propane, and A is the cross sectional area of the nanochannel. The vapor phase is approximated as an ideal gas. Differentiating the ideal gas law with respect to time for an isothermal system gives:

$$\frac{dl_B(t)}{dt} = \frac{RT}{AP_v(t)} \frac{dN_v(t)}{dt} - \frac{l_B}{P_v(t)} \frac{dP_v(t)}{dt}, \quad (6)$$

where R is the universal gas constant.

The differential equations (4) to (6) form a coupled system with three unknowns, $u_{liq}(t)$, $N_v(t)$ and $P_v(t)$. Solving the equations requires a boundary condition on $u_{liq}(t)$, $N_v(t)$, or $P_v(t)$. For the steady linear growth regime, the pressure inside the bubble column is assumed to be close to the saturation pressure, i.e., $P_v = P_{sat}$. By using this assumption, Eq. (6) is applied to predict dN_v/dt in the steady linear growth regime. The evaporation rate dN_v/dt is assumed to be constant for each experimental condition and matching that of the steady linear growth regime. The inset in Fig. 4a shows that the evaporation rate decreases from 2.02×10^{-13} to 0.99×10^{-13} mol/s as the temperature increases from 342.4 to 361.2 K (superheat decreases from 31.6 to 8.8 K).

The calculated value of dN_v/dt and the measured growth data $l_B(t)$ are applied in Eq.(5) to calculate the liquid velocity $u_{liq}(t)$. For the case shown in Fig. 3a, it is found that 89% of the liquid-vapor interface movement, $dl_B(t)/dt$, results from the liquid flow, $u_{liq}(t)$, and the remaining is due to evaporation, dN_v/dt . Similarly for the other nucleation conditions, the ratios are 90% (342.4 K), 88% (351.3 K), 86% (356.2 K) and 84% (361.2 K).

In the transient start-up regime, a high vapor pressure is required to counter the fluid inertia. The momentum equation, Eq.(4), with calculated $u_{liq}(t)$ is used here to predict P_v as a function of time. As shown in Fig 4b, P_v of the Type A test at $T = 346.3$ K is predicted to be as high as 14.7 MPa at initial and dropping sharply approaching a plateau level of 2.52 MPa in the steady linear growth regime. The transient regime of P_v agrees with the general trend observed in a previous study [22].

Predicted P_v at other temperature conditions are provided in the following section "Supplemental data".

S8 - Supplemental data

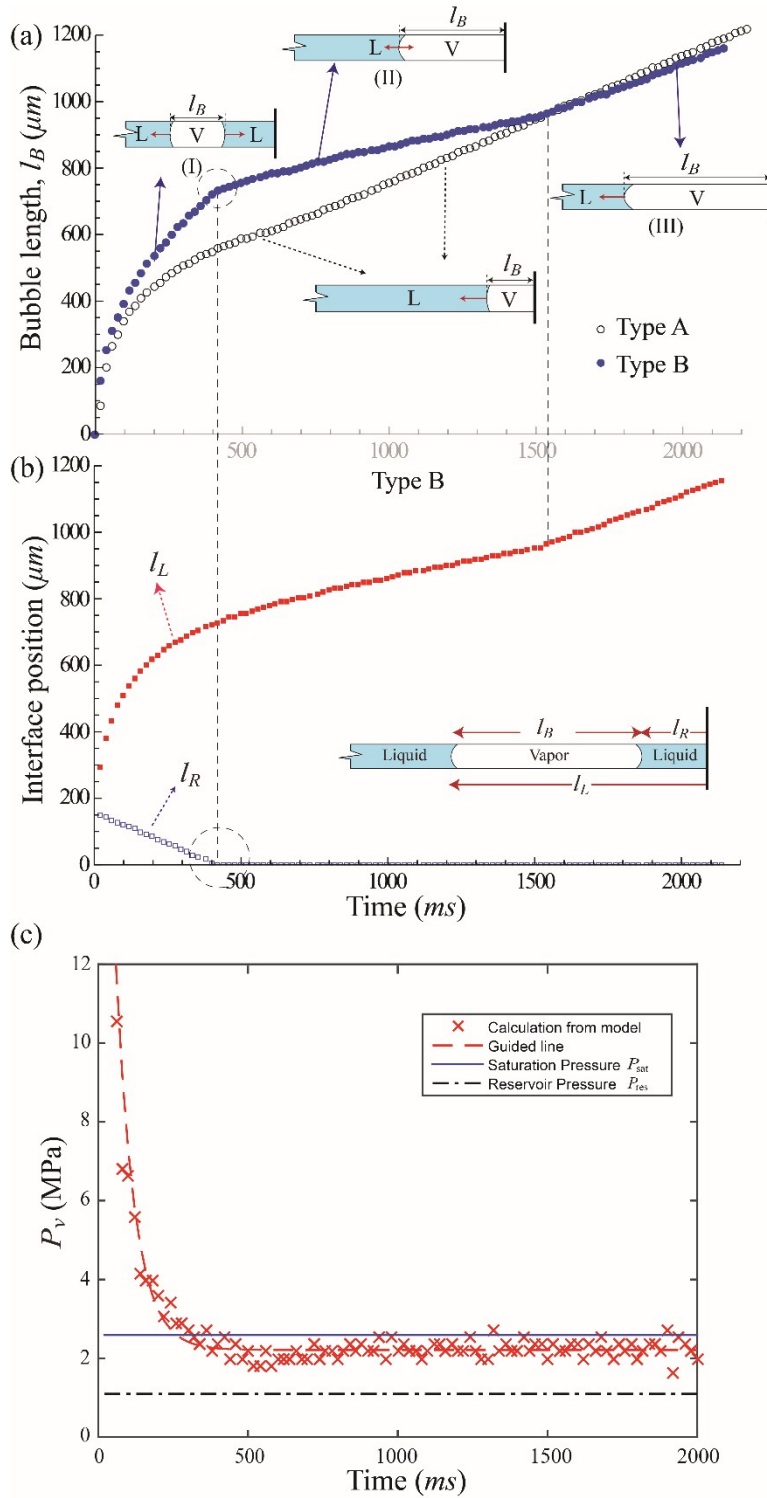


FIG. S7. Mechanisms of bubble column growth at $T_l = 342.4$ K and $P_l = 1.10$ MPa: a) Bubble length l_B versus time of Type A and B growth; b) Positions of left and right liquid-vapor interfaces, l_L and l_R , of Type B growth; c) Predicted bubble pressure P_v (Type A) during bubble column growth.

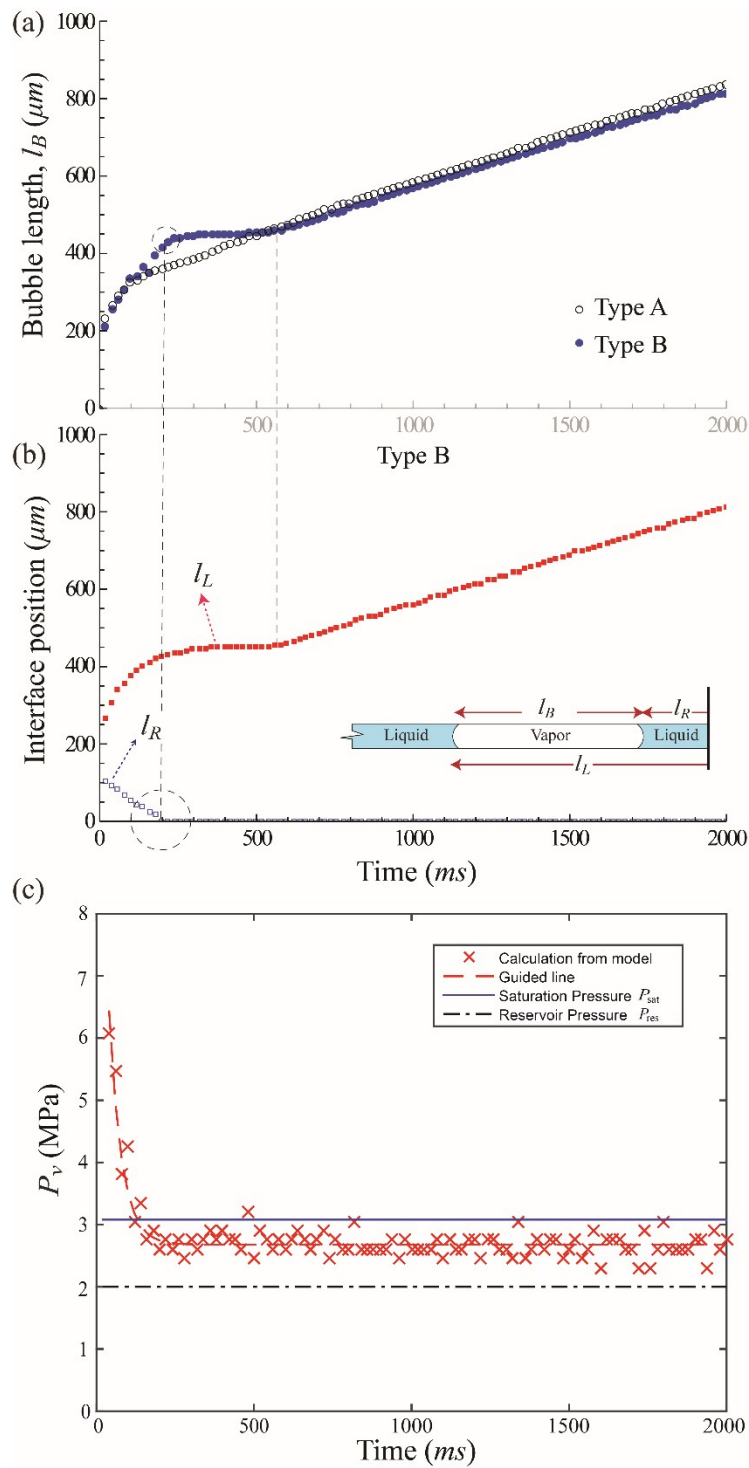


FIG. S8. Mechanisms of bubble column growth at $T_l = 351.3$ K and $P_l = 2.00$ MPa: a) Bubble length l_B versus time of Type A and B growth; b) Positions of left and right liquid-vapor interfaces, l_L and l_R , of Type B growth; c) Predicted bubble pressure P_v (Type A) during bubble column growth.

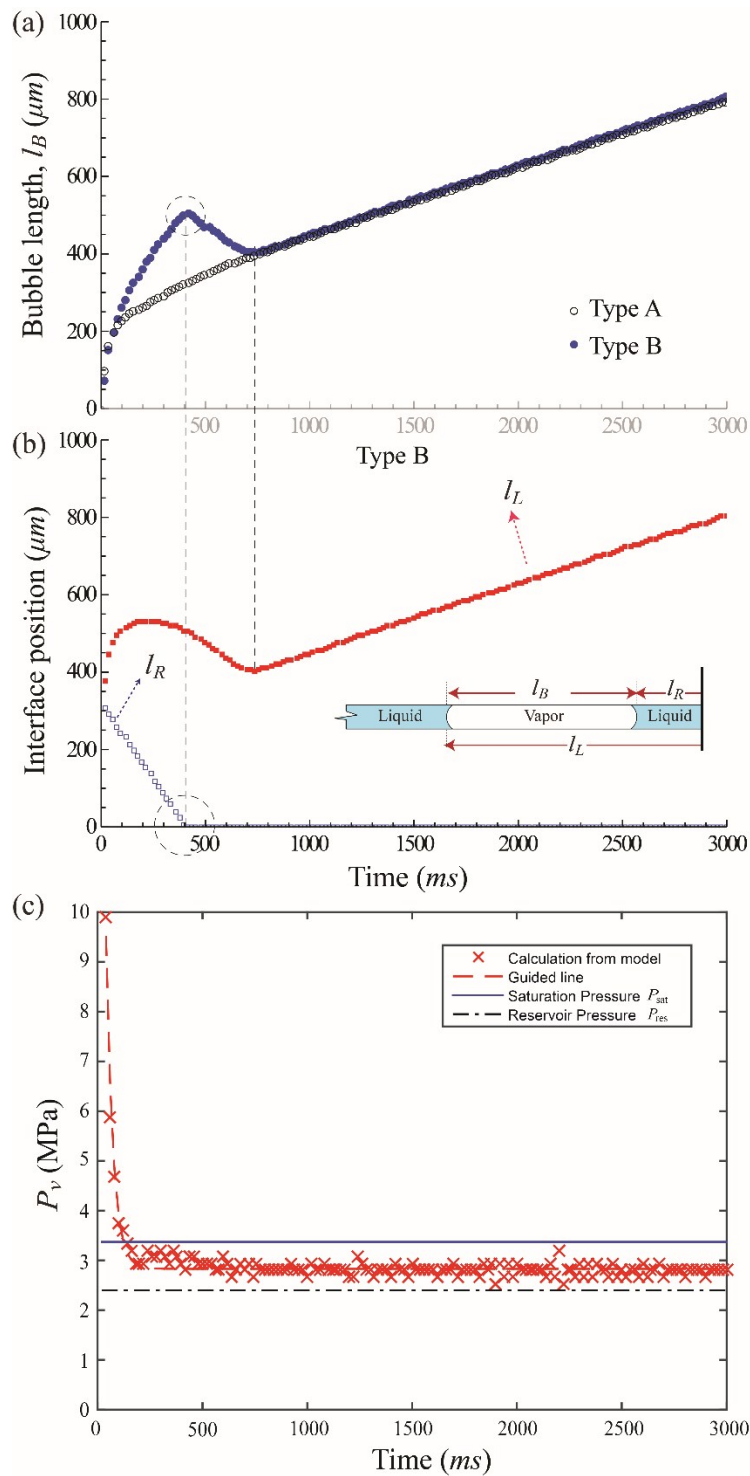


FIG. S9. Mechanisms of bubble column growth at $T_l = 356.2$ K and $P_l = 2.40$ MPa: a) Bubble length l_B versus time of Type A and B growth; b) Positions of left and right liquid-vapor interfaces, l_L and l_R , of Type B growth; c) Predicted bubble pressure P_v (Type A) during bubble column growth.

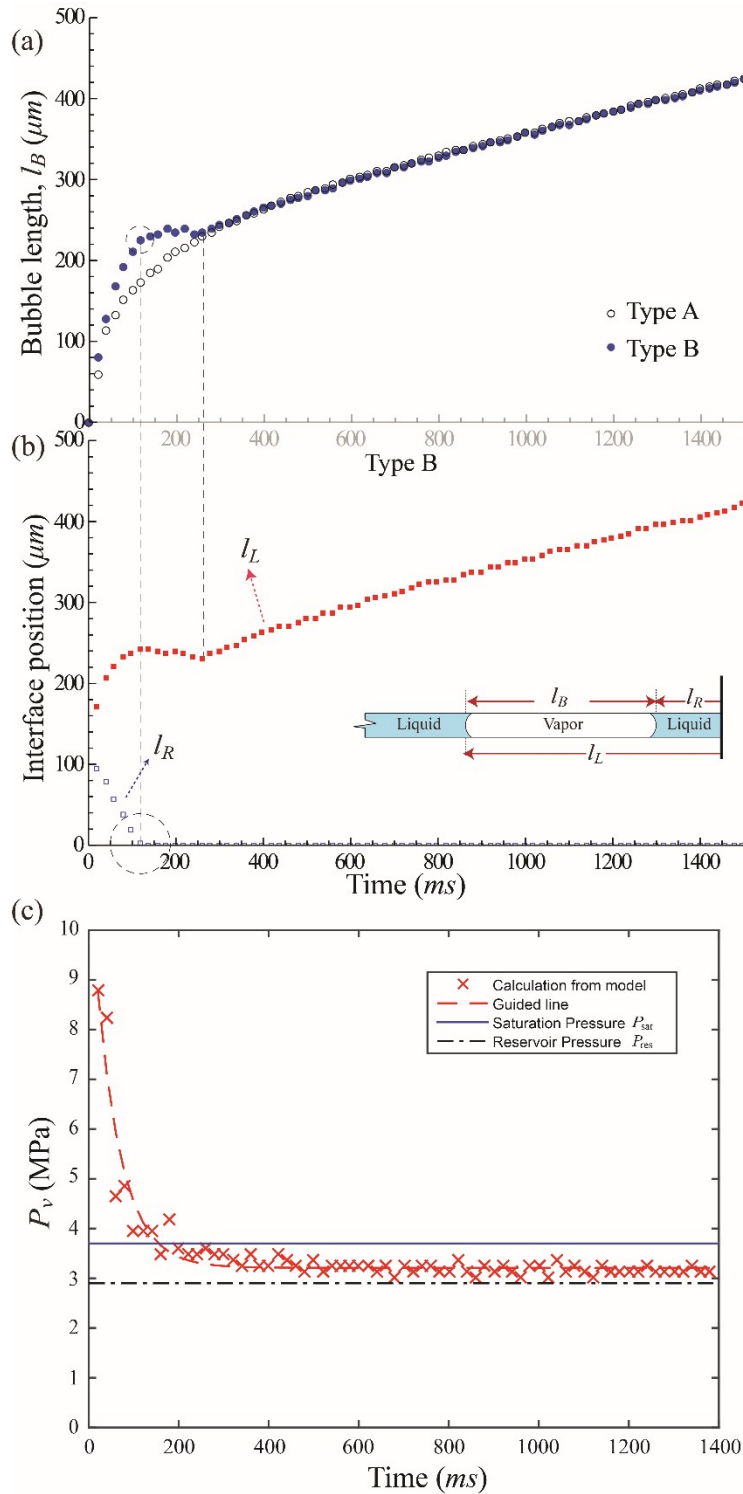


FIG. S10. Mechanisms of bubble column growth at $T_l = 361.2$ K and $P_l = 2.90$ MPa: a) Bubble length l_B versus time of Type A and B growth; b) Positions of left and right liquid-vapor interfaces, l_L and l_R , of Type B growth; c) Predicted bubble pressure P_v (Type A) during bubble column growth.

References

- [1] V. P. Carey, *Liquid-Vapor Phase-Change Phenomena* (Taylor & Francis Group, New York. Abingdon, 2008).
- [2] C. Sun, E. Can, R. Dijkink, D. Lohse, and A. Prosperetti, *J. Fluid Mech.* **632**, 5 (2009).
- [3] Frank M. White, *Viscous Fluid Flow* (McGraw-Hill, New York Etc., 1991).